









RESEARCH ARTICLE OPEN ACCESS

Morphology-Controlled Silica Nanoparticle Coatings for Transparent Radiative Cooling

Jefferson A. S. Lam¹ | Kishin Matsumori²  | Maximillian Theis³  | Alexander Berger³  | Nicole Böller³  | Qimeng Song³  | Matthieu Gresil¹  | Jacek J. Jasieniak¹  | Markus Retsch⁴ 

¹Department of Materials Science and Engineering, Faculty of Engineering, Monash University, Clayton, Australia | ²Institute of Microstructure Technology, Karlsruhe Institute of Technology, Eggenstein-Leopoldshafen, Germany | ³Physical Chemistry I, Department of Chemistry, Faculty of Biology, University of Bayreuth, Bayreuth, Germany | ⁴Physical Chemistry I, Department of Chemistry, Bavarian Polymer Institute, Bayreuth Center for Colloids and Interfaces, Bayreuther Institut für Makromolekülforschung, and Bavarian Center For Battery Technology (BayBatt), Faculty of Biology, University of Bayreuth, Bayreuth, Germany

Correspondence: Jefferson A. S. Lam (jefferson.lam@monash.edu) | Jacek J. Jasieniak (jacek.jasieniak@monash.edu) | Markus Retsch (rets@uni-bayreuth.de)

Received: 15 December 2025 | **Revised:** 15 April 2026 | **Accepted:** 27 April 2026

Keywords: coating | nanoparticle | passive radiative cooling | photovoltaics | transparent

ABSTRACT

In this study, transparent passive radiative cooling coatings are introduced by immobilizing solid and hollow silica (SiO₂) spheres on glass substrates. It is showcased that particle morphology within a sub-monolayer coating strongly influences visible and atmospheric window reflectance of glass. Solid and hollow-sphere particles of total diameter within the Mie regime reduce atmospheric window reflectance (R_{AW}) at the expense of higher visible reflectance (R_{VIS}). This trade-off is dependent on particle and core diameter. Solid particles with particle diameter >1000 nm can reduce the R_{AW} of glass by up to 65 %, though increase R_{VIS} by 25 %. Meanwhile, the use of hollow-sphere nanoparticles of similar diameters and thin shells (25–50 nm) can reduce the R_{AW} of glass by up to 35 % with minimal changes to R_{VIS} . These spectroscopic trends are validated numerically via both Mie theory and effective medium theory. The work demonstrates that hollow-sphere morphology is a valuable lever to control passive radiative cooling for various solar applications requiring transparency, such as coatings for windows or photovoltaic devices.

1 | Introduction

As average global temperatures reach new heights due to climate change, there is a growing need for sustainable cooling systems [1, 2]. Passive cooling technologies offer a zero-energy solution by drawing upon shading, ventilation, endothermic phase transitions, solar reflection, and infrared (IR) emission [3–5]. Among these, the latter two cooling mechanisms are particularly favorable for reducing weight and material use, versatility, and cost [6]. Surfaces covered by these passive radiative cooling (PRC) coatings can maintain lower temperatures than the surrounding environment by (1) reflecting sunlight, with wavelengths (λ) spanning 0.3–2.5 μm ; (2) re-emitting absorbed heat into the

cold outer space through Earth's atmospheric window (AW, $8 < \lambda < 13 \mu\text{m}$); and (3) minimizing absorption of downward atmospheric radiation (light reflected back onto the earth's surface by the atmosphere) (Figure 1a). Achieving strong passive cooling via coatings provides an opportunity to drastically reduce energy costs in buildings, transportation, and food storage, via application onto both new and existing systems [7].

The foundational studies that addressed PRC focused on simple bulk and hybrid material systems. These works spotlighted materials with: (1) strong solar reflectance (e.g. aluminum/silver foils); (2) broadband or selective infrared emittance (mainly polymeric materials, for example PVDF, PE, PDMS, PTFE, PMMA), and

This is an open access article under the terms of the [Creative Commons Attribution](https://creativecommons.org/licenses/by/4.0/) License, which permits use, distribution and reproduction in any medium, provided the original work is properly cited.

© 2026 The Author(s). *Advanced Materials Interfaces* published by Wiley-VCH GmbH

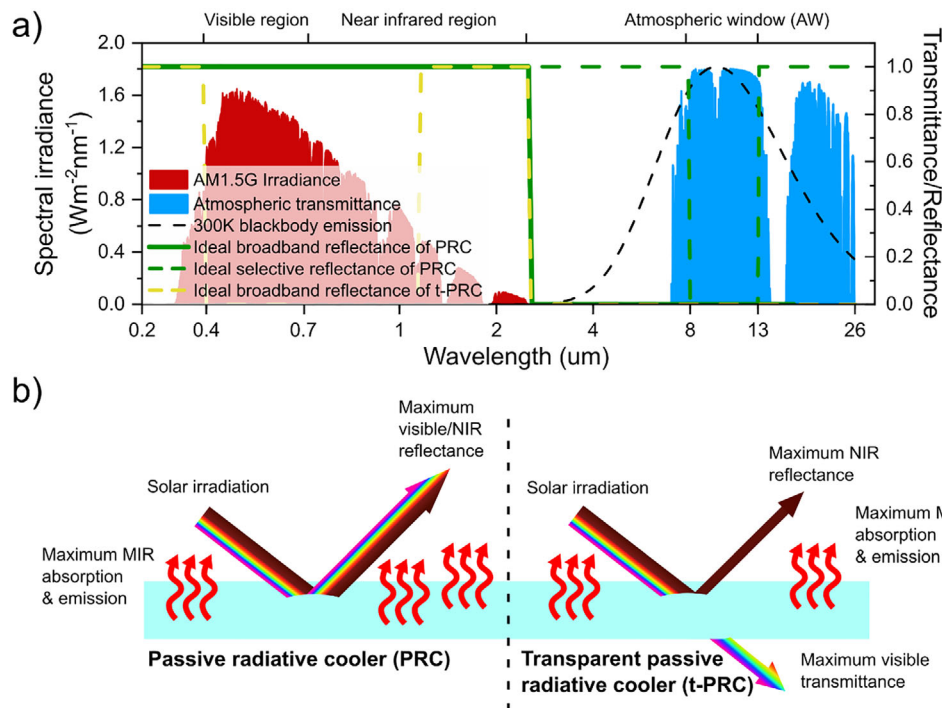


FIGURE 1 | Ideal requirements of non-transparent and transparent passive radiative coolers (PRC). (a) AM1.5G spectral irradiance and mid-infrared (commencing at 5.6 μm) atmospheric transmittance (measured at Gemini North Telescope, 1.0 mm water vapor column, AM1.5) (<https://www.gemini.edu/>). Overlaid is the 300 K blackbody emission, calculated using Planck's Law, and the ideal reflectance of transparent and non-transparent PRC. (b) Schematic representation of ideal light interactions of a typical passive radiative cooler vs. a transparent passive radiative cooler. The former seeks to maximize reflectance of solar irradiation while the latter seeks to allow only the visible wavelengths to pass through. Emission in the mid-infrared (MIR) range is ideally maximized in both cases.

(3) combined solar reflectance and infrared reflectance (mainly dielectrics, e.g. TiO_2 , BaSO_4 , SiO_2 , MgO , LiF) [7–13]. Many of these systems were able to achieve sub-ambient cooling during night-time, but the primary challenge was achieving this under $\sim 1000 \text{ W/m}^2$ of solar flux (i.e., during the day-time). The domineering approach to tackling this was to enhance the solar reflectivity, negating this flux. Typical material formulae have since been established to reach sub-ambient daytime cooling: utilizing either bilayer films of emissive polymers over highly reflective metal foils [14], or polymer nanocomposites in which polymer materials are embedded with strongly scattering inorganic oxide nanoparticles [15, 16]. Though notably, other unique strategies have also seen success, including materials that incorporate fibrillar structures [17, 18], dynamic cooling systems that actively reflect the dominant component of solar irradiation [19, 20], and the development of novel reflector materials [21]. Furthermore, recent research also integrates nanophotonic designs that enhance reflectivity, emissivity, and add functionalities such as adaptive cooling/heating, tunable wettability, and improved aesthetics [22–25]. Concepts to infer coloration without solar light absorption, for example, via structural coloration, require a fine balance between an improved optical impression and cooling performance [26]. Importantly, surrounding this development is the increasing consideration of scalability and sustainability, which are necessary qualities for the proliferation of the system.

Simultaneously, there has been growing interest in PRC materials, which are fully or partially transparent in the visible

region (i.e., 400–700 nm), for applications in windows, skylights, electronics, and photovoltaics. This completely shifts the design criteria as the reflection of visible light must now be minimized (Figure 1b). The reflection of near-infrared light ($3 < \lambda < 8 \mu\text{m}$) would ideally also be maximized, though it is not always necessary for strong cooling effects. This is because objects (e.g., PV cells) to be cooled are often at a higher temperature than ambient during operation—the nominal operating cell temperature (NOCT) of silicon solar cells is 40°C – 50°C [27]. It has been shown in the ideal scenario that a coating with unity AW emissivity can reduce the standard operating temperature of silicon cells by up to 18.3 K [28]. Such high emissivity materials rely on procuring precise photonic gratings on SiO_2 , PDMS, and PMMA with maximum temperature reductions of up to 13 K [29–31]. Minimizing the operating temperature of photovoltaic modules is vital, as efficiency declines, while degradation processes accelerate at higher temperatures. However, these transparent cooling systems often have complex designs, UV-sensitive thermoset matrices, poor recyclability, and require large material thicknesses (10–3000 μm), highlighting a need for more straightforward and more scalable solutions [32–36]. For example, Lee et al. showcase a PDMS/ SiO_2 aerogel metamaterial which exhibits temperature reductions of 5.1–6.2 K when thicknesses are increased from 30–3000 μm [33]. Thinner cooling materials have also been achieved through emissivity enhancements via a 10 μm coating of PDMS/dendritic SiO_2 as showcased by Yu et al. [36]. This film is found to greatly enhance a multi-layer cooling film (ITO/PET), resulting in maximum temperature reductions of up to 12.6 K compared to glass.

The idea of creating an “invisible” passive cooling coating, both in terms of minimal material usage and high optical transparency, relies on careful optical considerations. Jaramillo et al. uniquely showcased how passive cooling effects can be enhanced predominantly through surface phonon polariton effects [33]. They showed that coating a monolayer of silica particles with a diameter, d , of around $8\ \mu\text{m}$ on glass results in an average AW emissivity (ϵ_{AW}) of $> 98\%$, while maintaining a moderate average visible transmittance (T_{VIS}) of $> 82\%$. When covered by this monolayer, the temperature of a Si wafer was found to be $14\ \text{K}$ lower during the day. This enhancement of ϵ_{AW} is due to the higher absorption (as per Kirchhoff’s law) arising from propagating and higher-order surface phonon polaritons (SPhPs). These modes are generated within micro- and nano-structured silica, facilitating strong thermal absorbance, even within the Reststrahlen band, which would otherwise result in reflectance. Additionally, the introduction of a periodic lattice further enhances emissivity by enabling diffraction into the far-field. However, this configuration is limited by its high scattering in the visible region, and achieving such periodicity may be challenging at larger scales. It is known that dielectric particles of $d < \lambda$ support low-order mode resonances [37]. While less effective, these resonances can still support enhanced absorption while reducing Mie scattering. Furthermore, visible scattering may be reduced further by lowering the effective refractive index of the monolayer through hollow-sphere particles with less-dense packing. A key question thus emerges: can the use of SiO_2 nanoparticles or hollow-spheres ($0.2\text{--}1.2\ \mu\text{m}$) result in highly visible transparent coatings with high thermal emissivity?

In this work, we attempt to answer this question by applying disordered sub-monolayers of structurally controlled SiO_2 nanoparticles on glass. We examine and compare the effects of particle diameter, core diameter, and shell thickness on the visible and infrared spectroscopic properties of coated soda-lime glass substrates. This data is further validated through numerical methods employing Mie theory and effective medium theory. In doing so, we showcase how nanoparticle size and morphology influence the trade-off between visible transparency and mid-IR emissivity. We find that a sub-monolayer of SiO_2 nanoparticles applied on glass can significantly increase IR emissivity within the atmospheric window while preserving optical transparency—with the right particle geometries. We thereby show that harnessing Mie resonances in solid and hollow spheres can enhance passive radiative cooling effects whilst minimizing visible scattering. Given that such coatings are also capable of introducing superhydrophobicity with mechanical resilience [38], the work highlights the prospects of hollow silica spheres as a low-cost, scalable, and sustainable material strategy for imparting multifunctional properties to next-generation photovoltaics and other applications benefiting from passive cooling.

2 | Results and Discussion

2.1 | Sub-Monolayer Coating

Solid and hollow silica spherical particles were synthesized via a base-catalyzed Stöber process, whereby tetraethyl orthosilicate (TEOS) is hydrolyzed and condensed in ethanol with ammonia. Three sizes of silica spheres were synthesized: 320 , 473 , and

$1082\ \text{nm}$ in diameter. Silica hollow-spheres were formed by first synthesizing sacrificial cationic polystyrene cores (PS) via azobisisobutyronitrile (AIBN) initiated emulsion polymerization, with 2-Methacryloxyethyl trimethylammonium chloride (MTC) as the positively-charged co-monomer—according to previously developed procedures [39]. The size of the PS cores was determined via scanning electron microscopy (SEM): 130 , 202 , 323 , 493 , and $602\ \text{nm}$. Encasing these particles in silica involved the dispersion of these particles in ethanol with ammonia, and the subsequent dropwise addition of TEOS. By extracting particles during this shell formation, a range of shell thicknesses could be acquired. This was done using the $202\ \text{nm}$ PS cores to obtain 296 , 357 , 405 , 442 , 474 , and $497\ \text{nm}$ core-shell particles. The particle size distributions of all synthesized particles are described in Figure S1, and all particle geometry data are summarized in Table S1.

To form the disordered nanoparticle sub-monolayers, soda-lime glass slides with a poly(diallyl dimethylammonium chloride) (p-DADMAC) coating were immersed in an aqueous solution containing the solid and core-shell ($\text{SiO}_2/\text{PS-SiO}_2$) nanoparticles. Adhesion of the nanoparticles to the surface was achieved through electrostatic interactions between the positive ammonium groups and partially negative surface silanols. The core-shell nanoparticle coatings were further calcined at 500°C to remove the polystyrene cores and yield silica hollow spheres. The schematic shown in Figure 2 further illustrates this immersion coating process and the mechanism by which transparent passive cooling is achieved.

Through SEM, we observe that this facile immersion coating process results in disordered sub-monolayers of the various nanoparticles with low surface coverage ($\theta < 43\%$) (Figure 3). This bath deposition process during immersion is typically described by the random sequential adsorption (RSA) model, as electrostatics fix particles onto the surface. The formation of a multilayer is prevented by the electrostatic repulsion of previously immobilized particles and the like-charged objects still in dispersion. This model predicts a maximum coverage of 38.4% for monodisperse spheres [40]. It also suggests that larger spheres reach their coverage saturation much faster compared to smaller particles. Additional factors governing the achievable surface coverage are the solution ionic strength, particle density, concentration, dispersity, and surface roughness [41]. For example, it is known that particle deposition rates are strongly affected by particle size and ionic strength [42]. Compared to the ideal RSA model, we find marked deviations from the ideal behavior in our systems. First, the maximum surface coverage has not always been reached, particularly for particles with smaller diameters, indicating the necessity for a longer deposition time. More importantly, we observe a substantial degree of clustering. These clusters evolve during the drying process as strong capillary forces between the particles displace them from their initial position. Such aggregation effects could only be prevented through a solvent exchange process during drying or via particle fixation to the substrate. Nevertheless, the simple coating process used here yielded sub-monolayers of colloidal particles with a homogeneously disordered distribution. Visually, greater surface coverage results in higher visible opacity through increased scattering. This is explicitly seen in the insets of Figure 3. The scattering may also be enhanced by the clustering of particles

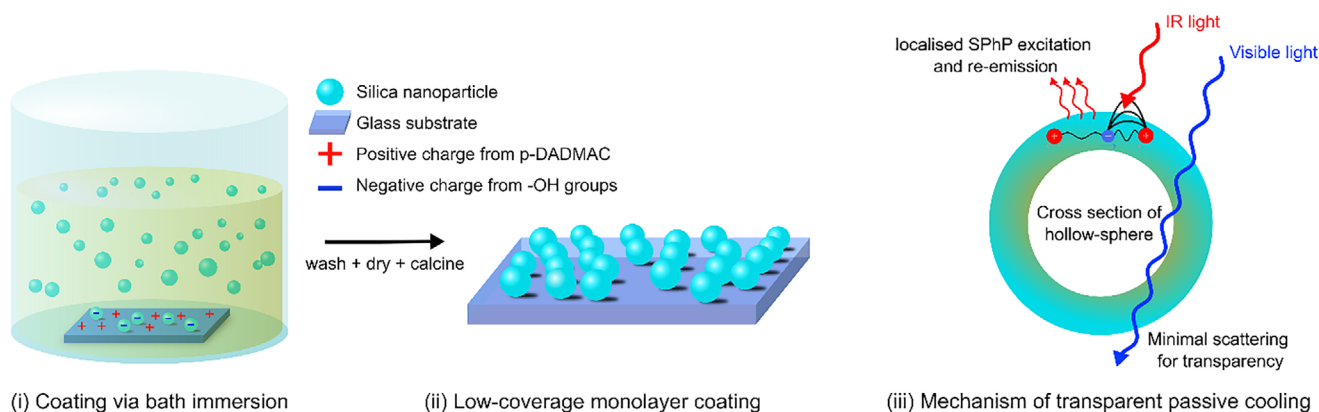


FIGURE 2 | Schematic of the fabrication process and mechanism for passive cooling of the silica sub-monolayer coatings. (i) Negatively charged silica nanoparticles are adsorbed onto the positively charged glass slide in a simple bath immersion process. (ii) This yielded the sub-monolayer coating on glass, with high visible transparency. (iii) The high absorption (resulting in high emission) in the atmospheric window (8–13 μm) is due to phonon-polariton effects. Hollow spheres provide a lower effective refractive index of the coating, thereby reducing backscattering in the visible region.

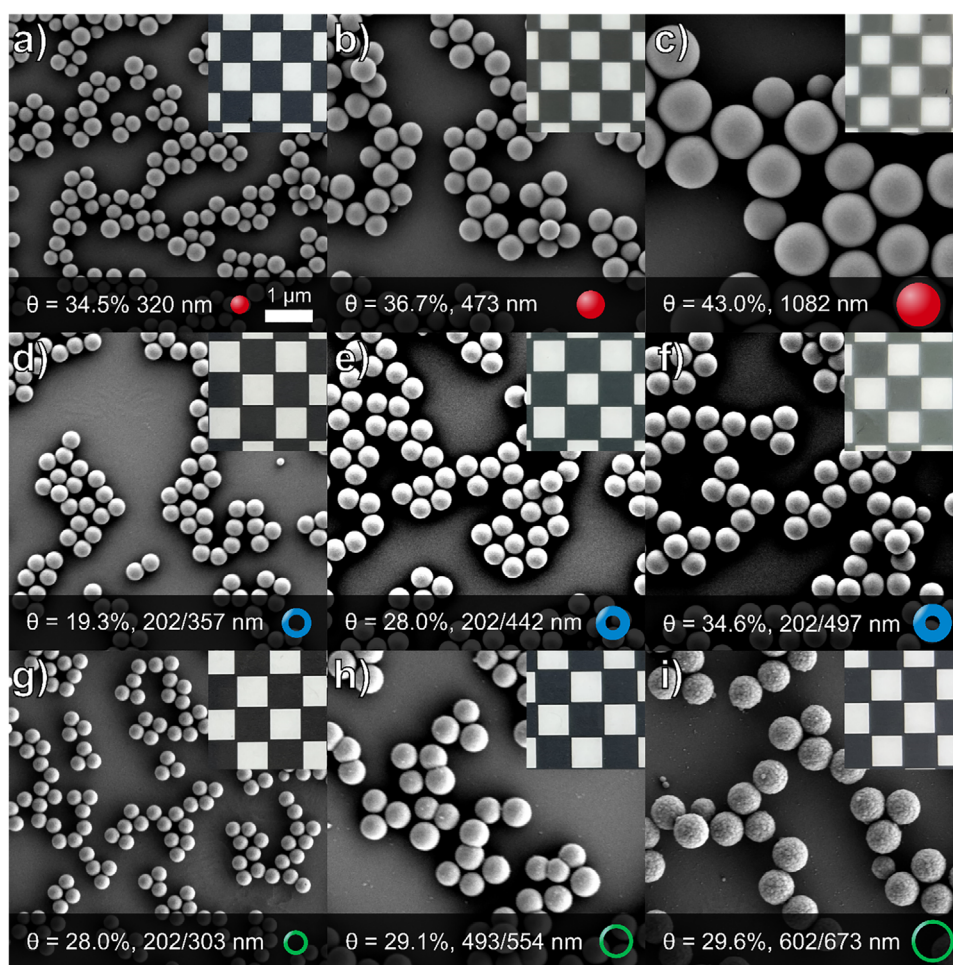


FIGURE 3 | Distribution and coverage of low-coverage silica nanoparticles sub-monolayers via SEM (10kx, 4.8 mm, 2 kV, 30 μm). Insets: Photograph of respective sub-monolayer coating on glass slides over a checkerboard backdrop (0.5 cm \times 0.5 cm per square). Percent coverage (θ) determined via binary image processing. Size measured via SEM ($n > 50$). (a–c) Solid silica nanoparticles. (d–f) Hollow-sphere nanoparticles with a constant core diameter of 202 nm. (g–i) Hollow-sphere nanoparticles with thin shells.

due to attractive capillary forces upon solvent evaporation in the drying process. The contrast of the checkerboard-patterned insets also serves as a visual indicator of optical clarity. Hollow-sphere nanoparticles with thin shells and a small total diameter appear to improve the clarity of the coating, likely due to a reduction in Mie scattering (Figure 3g,h).

2.2 | Spectroscopic Analysis and Cooling Performance

Soda-lime glass is transparent in the visible region due to its high optical bandgap, but interacts strongly with light in the mid- to far-infrared due to Si–O vibrational resonances [43]. Under these conditions, total reflectance (R) can be used to derive both T_{VIS} and ϵ_{AW} of glass. Here, the measured R of the solid and hollow-sphere sub-monolayer coatings on glass is compared with theoretical calculations (Figure 4). Averaged across the visible range, total reflectance (R_{VIS}) is preserved for all particle morphologies, remaining below 11.5% ($T_{VIS} = 88.5\%$). The highest reflectance was observed using the largest solid spheres (Figure 4a). Meanwhile, the use of smaller hollow-sphere nanoparticles exhibited a minor reduction in reflectance; for instance, the 303-nm diameter thin-shelled hollow-spheres yielded $R_{VIS} = 8.8\%$ (compared to 9.2% for bare glass) (Figure 4c).

The spectral trends in the visible range are compared to the backscattering efficiency (Q_{bsc}) calculated using Mie theory (Figure 4a,c,e). These calculations assume isolated silica spheres in air, neglecting multiple scattering effects, substrate interference, particle dispersity, and particle clustering—which are present in the experimental analysis. Further imperfections within the silica particle and silica shell, respectively, can lead to additional light scattering. The calculated backscattering profiles are found to be redshifted compared to experimentally obtained spectra. This is most evident in Figure 4c. Nevertheless, the general trends of the reflectance spectra are well captured, justifying the use of Mie theory for the morphology optimization discussed in Section 2.3. Additional Mie-calculation data (e.g., absorption spectra, resonance orders, etc.) are presented in Figures S4–S6.

Averaged across the atmospheric window, the total reflectance (R_{AW}) of coated substrates is reduced, with larger and solid particles having a greater effect (Figure 4b,d,f). The largest reduction is observed using the largest tested solid spheres ($d = 1082$ nm), with $R_{VIS-glass} = 5.6\%$ (vs. $R_{AW-glass} = 15\%$). This corresponding to $\epsilon_{AW} = 94.4\%$ ($\epsilon_{AW} = 100 - R_{AW}$). The magnitude of this reduction is less than that of the close-packed system of much larger, 8 μm , silica spheres ($\epsilon_{AW} > 98\%$), although it is still appreciable [33]. Hollow-sphere systems were not able to reach these emissivity values; however, thin-shelled hollow-spheres with $d < 350$ nm were able to reduce R_{AW} to 13%, corresponding to $\epsilon_{AW} > 87\%$ without sacrifice of visible transmittance.

The validity of these infrared results is also confirmed via numerical simulations. First, as $d \ll \lambda$ in the AW region, the effective permittivity of the monolayer is determined using effective medium theory [44]. Then, reflectance is calculated via the transfer matrix method using this effective permittivity, with the thickness given by the particle diameter (the details can be found in the Method section and Figure S3). We note that this

effective medium approach is a simplification, since the effective refractive index will assume a maximum along the z-direction at the particle's equator. Furthermore, considering the particle clustering observed in the lateral direction, patches of variable optical density are expected to contribute to the overall reflectance in the AW region, too. Deviations from the effective medium approach are expected to be strongest for the most efficient scatterers (solid spheres) and particles/particle clusters of the largest sizes. Despite these deficiencies, we find that the calculated reflectance captures the measured reflectance reasonably well for all particle morphologies. It confirms for all cases the reduced reflectance compared to bare glass (Figure 4b,d,f, smooth lines).

Solid sphere absorption increases with particle size due to the larger effective thickness of the coating. For particles with a constant core size, increasing shell thickness results in higher absorption due to both the effective thickness and absorption coefficient increasing (Figure S8). For hollow-sphere particles with thin shells, the effective absorption coefficient remains small even when particle size increases, so the reduction in reflectance is small (Figure S8). Interestingly, hollow spheres with thin shells exhibit two resonant conditions from the inner and outer surfaces of the shell. As the shell progressively thins, these two resonant modes hybridise, resulting in bonding and antibonding modes at around 9 and 8 μm , respectively (Figure S7). As absorption is weak, this results in little change in infrared reflectance. Evidently, the characteristic absorption due to localized phonon-polariton resonances is stronger for hollow-sphere particles with thicker SiO₂ shells and solid SiO₂ spheres. The larger polarizable volume of a solid particle allows for resonance modes to be excited—represented by a larger imaginary component of effective permittivity, ϵ'' .

We performed a proof-of-concept test to substantiate the added value of particle immobilization on the cooling performance. This involved coating glass slides (5 cm diameter) with 1082 nm solid spheres and 602 nm/673 nm (core/shell diameters) hollow spheres. To emulate the heat input to a solar cell, the coated glass slides were placed on top of a Si wafer. A thin layer of water was used to reduce interfacial reflection and to increase the thermal conductance. We used our indoor testing setup for assessing the radiative emittance improvement under nighttime conditions (no solar radiance input). We found a small temperature decrease between an uncoated glass slide and both particle-immobilized substrates (Figure S9a,b). Furthermore, we conducted an outdoor test, using the same experimental layout during the daytime. Here, we could also confirm the increase in cooling performance caused by the particle immobilization with a temperature reduction of about 1°C (Figure S9c,d). Both experiments demonstrate the added benefit of improving the emissivity via silica nanoparticle immobilization on a glass substrate. We could, however, not measure a significant difference between a solid and a hollow sphere.

2.3 | Morphology Dependence

The application of disordered, low-coverage solid and hollow-sphere silica nanoparticles can maintain high T_{VIS} and improve ϵ_{AW} when coated on glass. These two properties can be plotted against each other to show how particle morphology influences

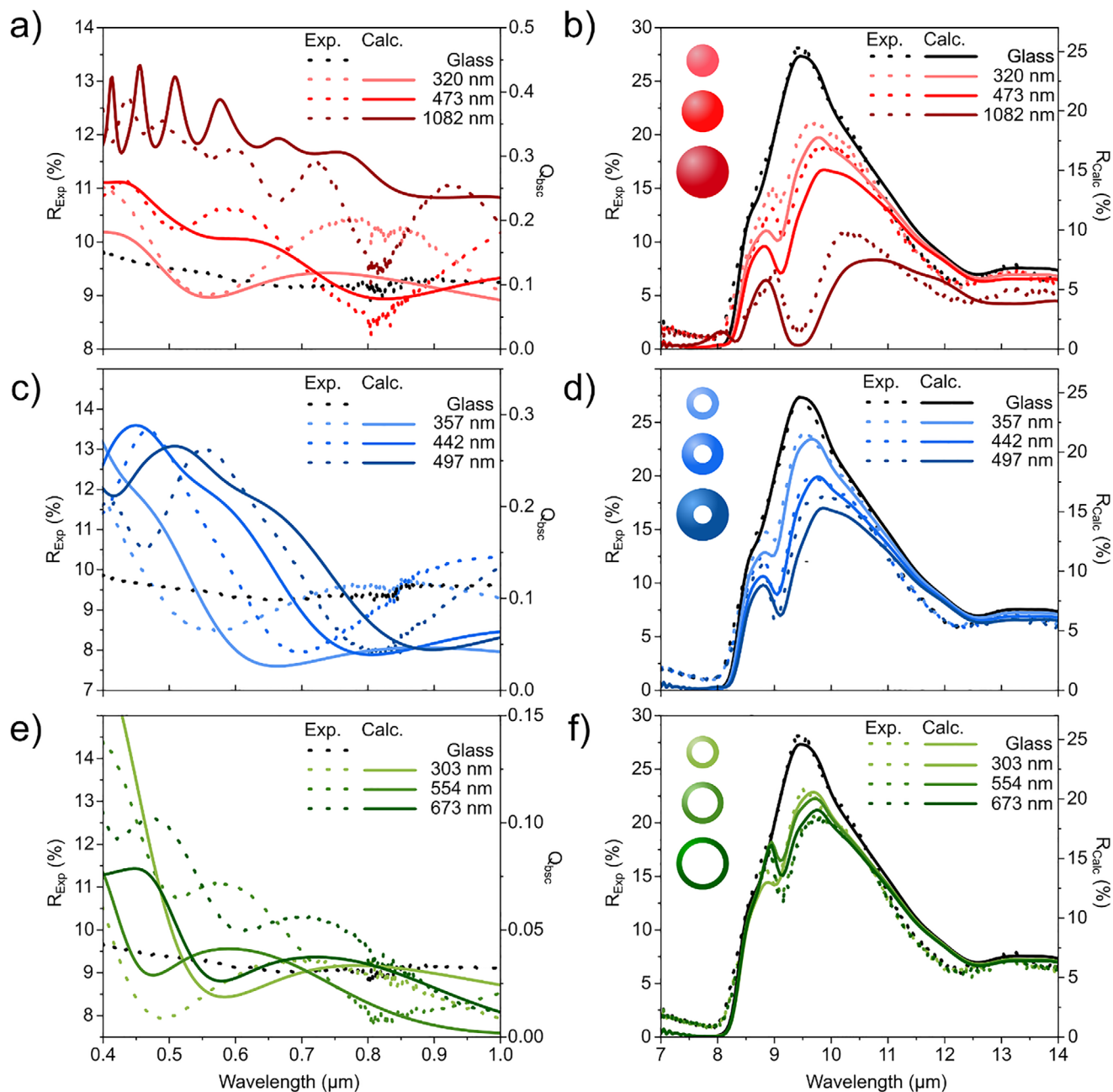


FIGURE 4 | Solar and mid-IR spectroscopic properties of the silica nanoparticle coatings of differing particle morphologies, and their comparisons to theory. UV-vis-NIR and mid-IR spectra, respectively for (a,b) solid silica particles (red); (c,d) hollow silica particles varying shell thickness (blue); (e,f) hollow silica particles varying core size (green).

these properties simultaneously (Figure 5a). It can be seen that a trade-off exists via the linear trend lines, with the negative gradients indicating that transparency is sacrificed for increased passive cooling effects. For example, as the size of solid sphere particles increases, the coating exhibits a significant reduction in AW reflectance and a slight increase in visible reflectance compared to uncoated glass. $R_{AW}/R_{AW-Glass} = 0.35$, $R_{VIS}/R_{VIS-Glass} = 1.2$ for 1082 nm particles. This corresponds to $\epsilon_{AW} = 94.6\%$, and a $T_{VIS} = 88.5\%$. Conversely, increasing particle size whilst maintaining a thin shell (i.e., increasing core size) reveals a much smaller trade-off. We find that by using ~ 300 nm, thin-shelled hollow-spheres, $R_{AW}/R_{AW-Glass} = 0.86$ and $R_{VIS}/R_{VIS-Glass} = 0.94$, which correspond to $\epsilon_{AW} = 87\%$, and a $T_{VIS} = 91.2\%$. Achieving

increased IR reflectance without sacrificing visible transmittance is ideal for PV applications. It is noted that the averaged values of reflectance shown in Figure 4 fall short of showcasing the wavelength dependent nature of the monolayer films (as seen in Figure S2). For example, when comparing coated samples to bare glass, one recognizes spectral ranges of reduced reflectance in almost all samples. This could be understood as an anti-reflective property in this spectral range, which can be of great value for the optimization toward a specific application, however is beyond the scope of this work.

The correlation between experiment and simulation (Figure 4) allows for a comprehensive comparison of a range of particle

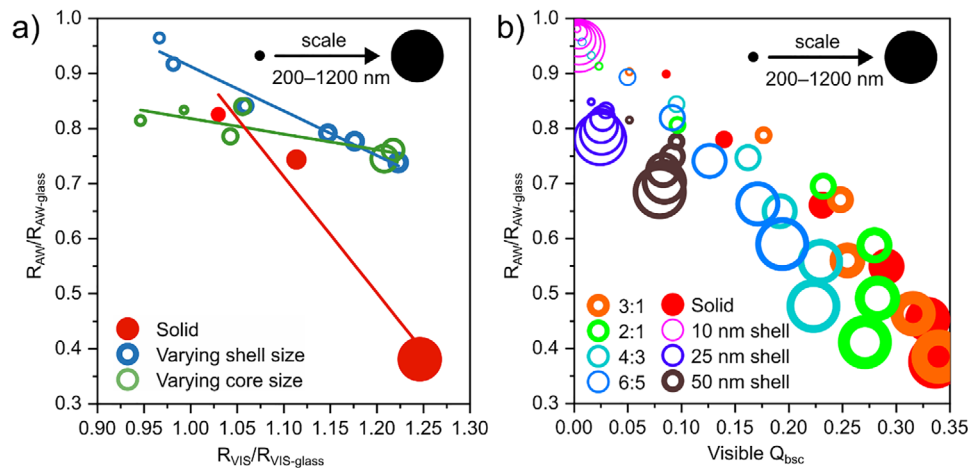


FIGURE 5 | Comparison of changes to atmospheric window reflectance, R_{AW} , and visible scattering for various particle morphologies. (a) Experimental data of normalized R_{AW} (8–13 μm) vs. R_{VIS} (400–700 nm). (b) Calculated data of normalized R_{AW} vs. average visible backscattering efficiency, Q_{bsc} . Ratios in legend refer to the particle-diameter to core-diameter ratio (i.e., 2:1 refers to the particle diameter being twice as large as the core size).

morphologies, including particle-diameter to core-diameter ratio and shell thickness (Figure 5b; note that this graph plots visible Q_{bsc} vs. normalized R_{AW}). The particles are seen to follow two general trends: (1) decreasing particle size, and (2) decreasing particle-diameter to core-diameter ratio reduces visible backscattering at the expense of infrared emissivity. This result confirms the initial hypothesis that both smaller particles and hollow-sphere particles can improve visible transmittance. Again, large solid particles have the largest reduction in infrared reflectance ($R_{AW}/R_{AW-Glass} = 0.35$), albeit with high visible backscattering ($R_{AW} = 0.33$). Interestingly, hollow spheres with 25 and 50 nm shells deviate slightly from the aforementioned trend, with backscattering efficiency consistently low ($Q_{bsc} < 0.1$). Increasing their particle sizes appears not to affect Q_{bsc} while reducing R_{AW} . We find that 1200 nm diameter particles with a shell thickness of 50 nm allow for appreciable reductions in $R_{AW}/R_{AW-Glass}$ (up to 0.66) while maintaining low backscattering ($Q_{bsc} = 0.07$). This would correspond to an $\epsilon_{AW} \approx 90\%$ with little change in visible transmittance. This is attributed to the shell becoming optically transparent (as shell thickness $\ll \lambda$) and simultaneously shifting the contributing backscattering modes outside the visible range [45].

The findings show that high T_{VIS} alongside increased ϵ_{AW} can be achieved by utilizing a sub-monolayer of solid or hollow-sphere silica nanoparticles—if particle morphology is appropriately tuned. Larger solid silica particle coatings support increased localized SPhP resonance, which enhances the absorption and emission of infrared light by up to 70%, but increases visible scattering by 15%, compared to uncoated glass. Alternatively, the use of hollow spheres can sustain strong solar light transmittance when thin shells (< 50 nm) are used, while also improving infrared emission by up to 40%. Pushing the particle size bigger boosts ϵ_{AW} by supporting SPhP resonances but increases backscattering, reducing T_{VIS} . Conversely, thin-shelled hollow spheres ($t < 50$ nm) can maintain glass-like T_{VIS} by reducing scattering contributions while retaining useful IR resonances. This creates two practical regimes: (i) transparency-first (thin-shelled hollow

spheres and low surface coverage) and (ii) cooling-first (larger dense spheres and higher surface coverage).

This coating design, if optimized further, has advantages over other PRC coatings due to its scalable bath immersion coating process, minimal material usage, and simple design. Furthermore, particle morphology can be tuned and selected according to the requirements of the end application. For example, applications that require high visible transparency, such as windows or photovoltaic glass, may benefit from particles within the transparency-first regime. From here, there are many avenues for further investigation, both experimentally and theoretically, such as the effect of surface coverage, larger particle sizes ($d > 1000$ nm), and maintaining thin shells ($t < 100$ nm), coating durability, and the demonstration of cooling at scale. These directions will be essential for optimizing the coating's performance in passive cooling applications requiring high visible transparency.

3 | Conclusion

This work demonstrates a sustainable route toward highly transparent passive radiative cooling by employing a sub-monolayer of silica nanoparticles on glass. This system leverages the vibrational modes of silica to boost absorption in the atmospheric window. By manipulating particle design, we identify an intrinsic trade-off between optical transparency and thermal emittance governed by morphology-dependent Mie resonances. While large solid spheres maximize interaction volumes to yield the highest emissivity ($>94\%$), they incur visible reflectance gains of around 25% due to increased backscattering. Conversely, small thin-shelled hollow spheres offered a strategic compromise, suppressing Mie scattering modes in the visible range while providing some enhancements in emissivity ($>87\%$). Validated by numerical simulations, these findings establish hollow silica spheres as a scalable, low-cost strategy for enhancing photovoltaics and other systems requiring passive thermal management and high optical transparency.

4 | Experimental Section/Methods

4.1 | Synthesis of Solid Silica Particles

Solid silica nanoparticles of three sizes were prepared via the Stöber process. In a 250 mL flask, 80 mL ethanol (Sigma-Aldrich), 10 mL MilliQ water (Millipore Direct Q3UV unit, Merck Millipore), 6 mL 35 % ammonia solution (Sigma-Aldrich), and 5 mL TEOS (added dropwise) (Sigma-Aldrich) were mixed and allowed to react for 12 h at room temperature.

4.2 | Synthesis of Hollow-sphere Silica Particles

Polystyrene (PS) nanoparticles were first synthesized as a sacrificial template via emulsion or dispersion (for > 400 nm particles) polymerization using 2-methacryloxyethyltrimethylammoniumchloride (MTC, Sigma-Aldrich), absolute ethanol (Sigma-Aldrich), and styrene (Sigma-Aldrich) as received. 2,2'-Azobis(2-methylpropionitril) (AIBN, Sigma-Aldrich) was recrystallized from ethanol before use. The details of this synthesis are described in more detail by Lechner et al. [37]. Silica shells were synthesized upon these sacrificial PS cores via a modified Stöber process. To create PS-SiO₂ core shell particles of varying shell thickness, 2 mL of an aqueous solution containing 10 wt. % 200 nm PS seed nanoparticles were added into a mixture of EtOH:H₂O:NH₃ at a molar ratio of 4.3:2.7:1. A solution of 100 % TEOS in ethanol was added last at a rate of 2.5 mL/h. The reaction was left to proceed for 6 h, and 10 mL was extracted every hour. Each extraction provided a solution for a certain shell thickness. The synthesis of core-shell nanoparticles of variable core size involved separate PS core syntheses by varying MTC addition. Each core particle was then coated with silica via the modified Stöber process described previously to provide approximately 30–50 nm shells.

4.3 | Bath Immersion Coatings

Glass slides (Epidea) were washed by sonication for 10 min, subsequently in 2 % Hellmanex solution, MilliQ water, and ethanol. The surface was positively charged via immersion in a petri dish bath containing 2 % poly(diallyldimethylammonium chloride) (p-DADMAC) (Sigma-Aldrich) for 2 h. Excess p-DADMAC was removed by washing with water. Following surface treatment, the glass slides were placed within a bath containing 0.5 wt. % nanoparticle solution (diluted in MilliQ water) for 20 min. The coated slides were rinsed five times by dipping into a beaker of water and then ethanol, before being lightly blown dry using a pressurized air gun. To obtain hollow-sphere silica particles, the PS cores were calcined at 500 °C for 12 h. For simulated outdoor cooling performance, 50 mm diameter borosilicate glass (1.1 mm thickness) was coated only with 1082 nm diameter solid SiO₂ spheres and 602/673 nm (core/shell dia.) particles.

4.4 | Characterization

Nanoparticle size prior to and following shell synthesis was determined using scanning electron microscopy (SEM) and a

MATLAB-based evaluation software. Surface coverage was also measured using SEM, via ImageJ threshold adjustment. Spectroscopic properties were measured using an Agilent Cary 5000 UV-vis-NIR spectrometer and a Bruker Vertex 70 FTIR spectrometer, each equipped with an integrating sphere. Calibration was performed with the Spectralon diffuse reflectance standard and Au mirror for UV-vis and MIR measurements, respectively. Cooling performance measurements were conducted within a customized indoor “dome” set-up (Figure S9a). Borosilicate glass coated with nanoparticles was placed on the surface of a Si wafer of equal diameter. The night-time cooling performance was determined by measuring the temperature of the Si wafer via thermocouple when placed within a highly mid-IR absorbing graphite hemisphere, cooled by liquid nitrogen (mimicking the cold-sink of space). Outdoor cooling performance is measured by placing this system under clear-sky conditions in Germany.

4.5 | Numerical Methods and Simulations

The backscattering of the nanoparticles in the visible region was calculated using Mie theory [44]. First, the scattered field of the nanoparticles was computed, and the backscattering was obtained by integrating the scattered power over the backward hemisphere. The obtained values were normalized by the geometric cross-section of the nanoparticles to determine the scattering efficiency. In this calculation, electric and magnetic modes up to the 10th order were included to accurately account for size-dependent effects. The refractive index of SiO₂ was taken from the literature [47].

To describe optical behavior in the mid-IR range, the reflection properties of the solid silica nanoparticle coatings were described using effective medium theory via the Bruggeman approximation, where f_p is the volume fraction of the particles in the coating, and ϵ_p , ϵ_{air} , ϵ_{eff} , are the dielectric constants of the particle, air, and the monolayer coating, respectively Equation (1).

$$f_p \frac{\epsilon_p - \epsilon_{eff}}{\epsilon_p + 2\epsilon_{eff}} + (1 - f_p) \frac{\epsilon_{air} - \epsilon_{eff}}{\epsilon_{air} + 2\epsilon_{eff}} = 0 \quad (1)$$

For solid silica nanoparticle coating, ϵ_p was simply taken from the dielectric constant of SiO₂ [48]. The dielectric constants of the coatings composed of the hollow-sphere particles were calculated in two steps. First, the effective dielectric constants of the hollow-sphere particles were determined using the Maxwell-Garnett approximation, in which each hollow sphere was approximated as a single solid particle. Equation (2).

$$\epsilon_{core-shell,eff} = \epsilon_{shell} \left(\frac{\epsilon_{core} + 2\epsilon_{shell} + 2f(\epsilon_{core} - \epsilon_{shell})}{\epsilon_{core} + 2\epsilon_{shell} - f(\epsilon_{core} - \epsilon_{shell})} \right), f = \frac{r_{core}^3}{r_{shell}^3} \quad (2)$$

Next, the obtained effective dielectric constants of the hollow-sphere particles $\epsilon_{core-shell}$ were substituted into ϵ_p in Equation (1) to calculate the effective permittivity of the coatings. f_p in Equation (1) was experimentally determined from the surface coverage data. Otherwise, a fixed coverage of 30 % was used. Reflectance was then calculated using the transfer matrix method, ϵ_{eff} , and the refractive index of a glass substrate [46]. The calculation process is schematically illustrated in Figure S3.

Acknowledgements

The authors are grateful for the support, contributions, and funding sources that facilitated this research. This work was made possible by the funding from the Australian Government through the Australian Research Council (ARC) under the Centre of Excellence scheme (CE170100026) and the International Research Training Group (IRTG) OPTEXC, Project no. 464648186 (German Research Foundation). The authors acknowledge support from the Keylab Electron and Optical Microscopy.

Open access funding enabled and organized by Projekt DEAL.

Funding

This work was supported by the Australian Government through the Australian Research Council (ARC) under the Centre of Excellence scheme (CE170100026). International Research Training Group (IRTG) OPTEXC, Project no. 464648186 (German Research Foundation).

Conflicts of Interest

The authors declare no conflicts of interest.

Data Availability Statement

All relevant data are contained within the article and/or the Supplementary Material. Further inquiries can be directed to the corresponding author.

References

1. IEA, Heating and Cooling Strategies in the Clean Energy Transition, (International Energy Agency, 2019).
2. IPCC, "Contribution of Working Groups I, II and III to the Sixth Assessment Report of the Intergovernmental Panel on Climate Change," *Climate Change 2023: Synthesis Report* (Intergovernmental Panel on Climate Change, 2023): 35–115.
3. H. Akeiber, P. Nejat, M. Z. A. Majid, et al., "A Review on Phase Change Material (PCM) For Sustainable Passive Cooling In Building Envelopes," *Renewable and Sustainable Energy Reviews* 60 (2016): 1470–1497, <https://doi.org/10.1016/j.rser.2016.03.036>.
4. D. Al-Shamkhee, A. B. Al-Aasam, A. H. Al-Waeli, G. Y. Abusaibaa, and H. Moria, "Passive Cooling Techniques For Ventilation: An Updated Review," *Renewable Energy and Environmental Sustainability* 7 (2022): 23, <https://doi.org/10.1051/rees/2022011>.
5. Y. Elaouzy and A. El Fadar, "Energy, economic and environmental benefits of integrating passive design strategies into buildings: A review," *Renewable and Sustainable Energy Reviews* 167 (2022): 112828, <https://doi.org/10.1016/j.rser.2022.112828>.
6. M. Zeyghami, D. Y. Goswami, and E. Stefanakos, "A Review Of Clear Sky Radiative Cooling Developments And Applications In Renewable Power Systems And Passive Building Cooling," *Solar Energy Materials and Solar Cells* 178 (2018): 115–128, <https://doi.org/10.1016/j.solmat.2018.01.015>.
7. B. Grocholski, "Cooling in a Warming World," *Science* 370, no. 6518 (2020): 776–777, <https://doi.org/10.1126/science.abf1931>.
8. B. Givoni, "Performance And Applicability Of Passive And Low-Energy Cooling Systems," *Energy and Buildings* 17, no. 3 (1991): 177–199, [https://doi.org/10.1016/0378-7788\(91\)90106-D](https://doi.org/10.1016/0378-7788(91)90106-D).
9. C. G. Granqvist and A. Hjortsberg, "Radiative Cooling To Low Temperatures: General Considerations And Application To Selectively Emitting SiO Films," *Journal of Applied Physics* 52, no. 6 (1981): 4205–4220, <https://doi.org/10.1063/1.329270>.
10. P. Berdahl, "Radiative Cooling With MgO and/or LiF Layers," *Applied Optics* 23, no. 3 (1984): 370–372, <https://doi.org/10.1364/AO.23.000370>.

11. T. M. J. Nilsson and G. A. Niklasson, "Radiative Cooling During The Day: Simulations And Experiments On Pigmented Polyethylene Cover Foils," *Solar Energy Materials and Solar Cells* 37, no. 1 (1995): 93–118, [https://doi.org/10.1016/0927-0248\(94\)00200-2](https://doi.org/10.1016/0927-0248(94)00200-2).
12. C. G. Granqvist, "Radiative Heating And Cooling With Spectrally Selective Surfaces," *Applied Optics* 20, no. 15 (1981): 2606–2615, <https://doi.org/10.1364/AO.20.002606>.
13. B. Orel, M. K. Gunde, and A. Krainer, "Radiative Cooling Efficiency Of White Pigmented Paints," *Solar Energy* 50, no. 6 (1993): 477–482, [https://doi.org/10.1016/0038-092X\(93\)90108-Z](https://doi.org/10.1016/0038-092X(93)90108-Z).
14. A. P. Raman, M. A. Anoma, L. Zhu, E. Rephaeli, and S. Fan, "Passive Radiative Cooling Below Ambient Air Temperature Under Direct Sunlight," *Nature* 515, no. 7528 (2014): 540–544, <https://doi.org/10.1038/nature13883>.
15. L. Cai, A. Y. Song, W. Li, et al., "Spectrally Selective Nanocomposite Textile for Outdoor Personal Cooling," *Advanced Materials* 30, no. 35 (2018): 1802152, <https://doi.org/10.1002/adma.201802152>.
16. S. Park, S. K. Pal, T. Outouat, and G. Kim, "Radiative-Cooling Composites With Enhanced Infrared Emissivity by Structural Infrared Scattering Through Indium Tin Oxide Nanoparticles in a Polymer Matrix," *ACS Applied Materials & Interfaces* 15, no. 12 (2023): 16026–16033, <https://doi.org/10.1021/acsami.3c00143>.
17. B. Zhu, W. Li, Q. Zhang, et al., "Subambient Daytime Radiative Cooling Textile Based On Nanoprocessed Silk," *Nature Nanotechnology* 16, no. 12 (2021): 1342–1348, <https://doi.org/10.1038/s41565-021-00987-0>.
18. F. Xie, W. Jin, J. R. Nolen, et al., "Subambient Daytime Radiative Cooling Of Vertical Surfaces," *Science* 386, no. 6723 (2024): 788–794, <https://doi.org/10.1126/science.adn2524>.
19. B. Bhatia, A. Leroy, Y. Shen, et al., "Passive Directional Sub-Ambient Daytime Radiative Cooling," *Nature Communications* 9, no. 1 (2018): 5001, <https://doi.org/10.1038/s41467-018-07293-9>.
20. B. Zhao, K. Lu, M. Hu, et al., "Sub-Ambient Daytime Radiative Cooling Based On Continuous Sunlight Blocking," *Solar Energy Materials and Solar Cells* 245 (2022): 111854, <https://doi.org/10.1016/j.solmat.2022.111854>.
21. Y. Yang, L. Long, S. Meng, et al., "Bulk Material Based Selective Infrared Emitter For Sub-Ambient Daytime Radiative Cooling," *Solar Energy Materials and Solar Cells* 211 (2020): 110548, <https://doi.org/10.1016/j.solmat.2020.110548>.
22. Y. Zhai, Y. Ma, S. N. David, et al., "Scalable-Manufactured Randomized Glass-Polymer Hybrid Metamaterial For Daytime Radiative Cooling," *Science* 355, no. 6329 (2017): 1062–1066, <https://doi.org/10.1126/science.aai7899>.
23. C. Zou, G. Ren, M. M. Hossain, et al., "Metal-Loaded Dielectric Resonator Metasurfaces for Radiative Cooling," *Advanced Optical Materials* 5, no. 20 (2017): 1700460, <https://doi.org/10.1002/adom.201700460>.
24. Q. Zhang, S. Wang, X. Wang, et al., "Recent Progress in Day-time Radiative Cooling: Advanced Material Designs and Applications," *Small Methods* 6, no. 4 (2022): 2101379, <https://doi.org/10.1002/smt.202101379>.
25. X. Yu, J. Chan, and C. Chen, "Review of Radiative Cooling Materials: Performance Evaluation and Design Approaches," *Nano Energy* 88 (2021): 106259, <https://doi.org/10.1016/j.nanoen.2021.106259>.
26. T. Yu, R. Liu, Z. Yang, S. Yang, Z. Ye, and J. Lu, "Color Design for Daytime Radiative Cooling: Fundamentals and Approaches," *Applied Energy* 377 (2025): 124436, <https://doi.org/10.1016/j.apenergy.2024.124436>.
27. IEC 61215-1-3, Terrestrial Photovoltaic (PV) Modules—Design Qualification and Type Approval—Part 1–3: Special Requirements for Testing of Thin-Film Amorphous Silicon Based Photovoltaic (PV) Modules, (International Electrotechnical Commission, 2021).
28. L. Zhu, A. Raman, K. X. Wang, M. A. Anoma, and S. Fan, "Radiative Cooling Of Solar Cells," *Optica* 1, no. 1 (2014): 32–38, <https://doi.org/10.1364/OPTICA.1.000032>.

29. L. Zhu, A. P. Raman, and S. Fan, "Radiative Cooling Of Solar Absorbers Using A Visibly Transparent Photonic Crystal Thermal Blackbody," *Proceedings of the National Academy of Sciences* 112, no. 40 (2015): 12282–12287, <https://doi.org/10.1073/pnas.1509453112>.
30. M. Kim, D. Lee, S. Son, Y. Yang, H. Lee, and J. Rho, "Visibly Transparent Radiative Cooler under Direct Sunlight," *Advanced Optical Materials* 9, no. 13 (2021): 2002226, <https://doi.org/10.1002/adom.202002226>.
31. Y. Zhan, H. Yin, J. Wang, and C. Fan, "Enhanced Performance Of Diurnal Radiative Cooling For Solar Cells Based On A Grating-Textured PDMS Photonic Structure," *Materials Today Communications* 35 (2023): 106117, <https://doi.org/10.1016/j.mtcomm.2023.106117>.
32. J. Jaramillo-Fernandez, G. L. Whitworth, J. A. Pariente, et al., "A Self-Assembled 2D Thermofunctional Material for Radiative Cooling," *Small* 15, no. 52 (2019): 1905290, <https://doi.org/10.1002/smll.201905290>.
33. C. Ziming, W. Fuqiang, G. Dayang, L. Huaxu, and S. Yong, "Low-Cost Radiative Cooling Blade Coating With Ultrahigh Visible Light Transmittance And Emission Within An "Atmospheric Window"," *Solar Energy Materials and Solar Cells* 213 (2020): 110563, <https://doi.org/10.1016/j.solmat.2020.110563>.
34. K. W. Lee, W. Lim, M. S. Jeon, et al., "Visibly Clear Radiative Cooling Metamaterials for Enhanced Thermal Management in Solar Cells and Windows," *Advanced Functional Materials* 32, no. 1 (2022): 2105882, <https://doi.org/10.1002/adfm.202105882>.
35. K. W. Lee, J. Yi, M. K. Kim, and D. R. Kim, "Transparent Radiative Cooling Cover Window For Flexible And Foldable Electronic Displays," *Nature Communications* 15, no. 1 (2024): 4443, <https://doi.org/10.1038/s41467-024-48840-x>.
36. T. Yu, R. Liu, X. Wang, et al., "Transparent Radiative Cooling Films Based on Dendritic Silica for Room Thermal Management," *Carbon Neutralization* 4, no. 4 (2025): 70020, <https://doi.org/10.1002/cnl2.70020>.
37. X. Fan, W. Zheng, and D. J. Singh, "Light Scattering And Surface Plasmons On Small Spherical Particles," *Light: Science & Applications* 3, no. 6 (2014): e179–e179, <https://doi.org/10.1038/lsa.2014.60>.
38. X. Deng, L. Mammen, Y. Zhao, et al., "Transparent, Thermally Stable and Mechanically Robust Superhydrophobic Surfaces Made from Porous Silica Capsules," *Advanced Materials* 23, no. 26 (2011): 2962–2965, <https://doi.org/10.1002/adma.201100410>.
39. A. M. Lechner, T. Feller, Q. Song, et al., "Scalable Synthesis of Smooth PS@TiO₂ Core-shell and TiO₂ Hollow Spheres in the (sub) Micron Size Range: Understanding Synthesis and Calcination Parameters," *Colloid and Polymer Science* 298, no. 7 (2020): 867–878, <https://doi.org/10.1007/s00396-020-04626-3>.
40. P. Meakin and R. Jullien, "Random Sequential Adsorption Of Spheres Of Different Sizes," *Physica A: Statistical Mechanics and its Applications* 187, no. 3 (1992): 475–488, [https://doi.org/10.1016/0378-4371\(92\)90006-C](https://doi.org/10.1016/0378-4371(92)90006-C).
41. J. C. Fernández-Toledano, A. Moncho-Jordá, F. Martínez-López, and R. Hidalgo-Álvarez, "Theory for Interactions Between Particles in Monolayers," in *Colloidal Particles at Liquid Interfaces*, eds. B. P. Binks and T. S. Horozov (Cambridge University Press, 2006): 108–151, <https://doi.org/10.1017/CBO9780511536670>.
42. M. Elimelech, "Effect of Particle Size on the Kinetics of Particle Deposition under Attractive Double Layer Interactions," *Journal of Colloid and Interface Science* 164, no. 1 (1994): 190–199, <https://doi.org/10.1006/jcis.1994.1157>.
43. M. Rubin, "Optical Properties Of Soda Lime Silica Glasses," *Solar Energy Materials* 12 (1985): 275–288, [https://doi.org/10.1016/0165-1633\(85\)90052-8](https://doi.org/10.1016/0165-1633(85)90052-8).
44. D. Werdehausen, I. Staude, S. Burger, et al., "Design Rules For Customizable Optical Materials Based On Nanocomposites," *Optical Materials Express* 8, no. 11 (2018): 3456–3469, <https://doi.org/10.1364/OME.8.003456>.
45. M. Retsch, M. Schmelzeisen, H.-J. Butt, and E. L. Thomas, "Visible Mie Scattering in Nonabsorbing Hollow Sphere Powders," *Nano Letters* 11, no. 3 (2011): 1389–1394, <https://doi.org/10.1021/nl2002445>.
46. C. F. Bohren and D. R. Hoffman, "Absorption and Scattering by a Sphere," in *Absorption and Scattering of Light by Small Particles*. (John Wiley and Sons, 1998): 82–129.
47. I. H. Malitson, "Interspecimen Comparison of the Refractive Index of Fused Silica," *Journal of the Optical Society of America* 55, no. 10 (1965): 1205–1209, <https://doi.org/10.1364/JOSA.55.001205>.
48. R. Kitamura, L. Pilon, and M. Jonasz, "Optical Constants Of Silica Glass From Extreme Ultraviolet To Far Infrared At Near Room Temperature," *Applied Optics* 46, no. 33 (2007): 8118–8133, <https://doi.org/10.1364/AO.46.008118>.

Supporting Information

Additional supporting information can be found online in the Supporting Information section.

Supporting File: admi70524-sup-0001-SuppMat.docx.